

# UC Irvine

## UC Irvine Previously Published Works

### Title

Looseness Identification of Track Fasteners Based on Ultra-Weak FBG Sensing Technology and Convolutional Autoencoder Network

### Permalink

<https://escholarship.org/uc/item/4jq321md>

### Journal

Sensors, 22(15)

### ISSN

1424-8220

### Authors

Li, Sheng  
Jin, Liang  
Jiang, Jinpeng  
[et al.](#)

### Publication Date

2022

### DOI

10.3390/s22155653


### Copyright Information

This work is made available under the terms of a Creative Commons Attribution License, available at <https://creativecommons.org/licenses/by/4.0/>

Peer reviewed

## Article

# Looseness Identification of Track Fasteners Based on Ultra-Weak FBG Sensing Technology and Convolutional Autoencoder Network

Sheng Li <sup>1</sup>, Liang Jin <sup>2</sup>, Jinpeng Jiang <sup>1</sup>, Honghai Wang <sup>1</sup>, Qiuming Nan <sup>1,\*</sup> and Lizhi Sun <sup>3</sup>

<sup>1</sup> National Engineering Research Center of Fiber Optic Sensing Technology and Networks, Wuhan University of Technology, Wuhan 430070, China; lisheng@whut.edu.cn (S.L.); jiangjp2812@whut.edu.cn (J.J.); wanghh@whut.edu.cn (H.W.)

<sup>2</sup> School of Information Engineering, Wuhan University of Technology, Wuhan 430070, China; jl1290787604@whut.edu.cn

<sup>3</sup> Department of Civil and Environmental Engineering, University of California, Irvine, CA 92697-2175, USA; lsun@uci.edu

\* Correspondence: nqm0723@whut.edu.cn

**Abstract:** Changes in the geological environment and track wear, and deterioration of train bogies may lead to the looseness of subway fasteners. Identifying loose fasteners randomly distributed along the subway line is of great significance to avoid train derailment. This paper presents a convolutional autoencoder (CAE) network-based method for identifying fastener loosening features from the distributed vibration responses of track beds detected by an ultra-weak fiber Bragg grating sensing array. For an actual subway tunnel monitoring system, a field experiment used to collect the samples of fastener looseness was designed and implemented, where a crowbar was used to loosen or tighten three pairs of fasteners symmetrical on both sides of the track within the common track bed area and the moving load of a rail inspection vehicle was employed to generate 12 groups of distributed vibration signals of the track bed. The original vibration signals obtained from the on-site test were converted into two-dimensional images through the pseudo-Hilbert scan to facilitate the proposed two-stage CAE network with acceptable capabilities in feature extraction and recognition. The performance of the proposed methodology was quantified by accuracy, precision, recall, and F1-score, and displayed intuitively by t-distributed stochastic neighbor embedding (t-SNE). The raster scan and the Hilbert scan were selected to compare with the pseudo-Hilbert scan under a similar CAE network architecture. The identification performance results represented by the four quantification indicators (accuracy, precision, recall, and F1-score) based on the scan strategy in this paper were at least 23.8%, 9.5%, 20.0%, and 21.1% higher than those of the two common scan methods. As well as that, the clustering visualization by t-SNE further verified that the proposed approach had a stronger ability in distinguishing the feature of fastener looseness.

**Keywords:** feature identification; track fastener looseness; distributed vibration; convolutional autoencoder network; pseudo-Hilbert scan; ultra-weak fiber optic Bragg grating



**Citation:** Li, S.; Jin, L.; Jiang, J.; Wang, H.; Nan, Q.; Sun, L. Looseness Identification of Track Fasteners Based on Ultra-Weak FBG Sensing Technology and Convolutional Autoencoder Network. *Sensors* **2022**, *22*, 5653. <https://doi.org/10.3390/s22155653>

**Academic Editors:**

Michele Arturo Caponero, Cátia Sofia Jorge Leitão and Daniela Lo Presti

Received: 5 July 2022

Accepted: 26 July 2022

Published: 28 July 2022

**Publisher's Note:** MDPI stays neutral with regard to jurisdictional claims in published maps and institutional affiliations.



**Copyright:** © 2022 by the authors. Licensee MDPI, Basel, Switzerland. This article is an open access article distributed under the terms and conditions of the Creative Commons Attribution (CC BY) license (<https://creativecommons.org/licenses/by/4.0/>).

## 1. Introduction

The characteristics of small space, long mileage, and difficulty in personnel evacuation determine that it is more challenging to safeguard the underground structure of the subway than the ground building. To ensure subway safety, a wide range of research efforts has been undertaken in the fields of subway fires [1–3], structural safety [4–7], and illegal invasion [8–12]. Among the objects of concern in the field of structural safety monitoring, the track used to guide the train and bear the moving loads transmitted by the wheels plays a vital role in the operation of the subway. In the absence of extensive and meticulous inspection and maintenance, the long-term repeated impact of subway trains will undoubtedly reduce the strength and stability of the track structure. In severe cases, the vibration of

the track system caused by the interaction between the train and the track will cause the rail fasteners to loosen, rupture, and even lead to catastrophic derailment accidents [13]. In related reports on train derailment, the research status and major problems were reviewed in [14]. For the detection method aiming for preventative maintenance, the traditional inspection regime is usually labor-intensive and can be significantly expensive for the rail operator [15]. In addition to manual-based periodic inspection methods, Ikshwaku et al. [16] reported the feasibility of using drones to monitor railway-related infrastructure, which is obviously not suitable for monitoring subway lines in tunnels. Moreover, the image-based detection techniques were compared in [17], which are susceptible to the interior environment of the subway tunnel.

Since the tracks are fastened to the track bed by fasteners, it is possible to obtain the fastener condition by monitoring the structural vibration response of the track bed caused by passing trains in terms of the relationship between the vibration response and the structural state. According to the reports in [11,12,18], the ultra-weak fiber optic Bragg grating (FBG) sensing technology [19] is a feasible way to collect the distributed vibration of the track bed along the subway line. To avoid the vibration characteristics caused by fastener loosening being submerged in the vibration response of the track bed, feature extraction should be the most intuitive idea that can improve the effectiveness and efficiency of the fastener's looseness identification. Numerous reports [20–23] have demonstrated the good performance of the convolutional neural network (CNN) in various application domains. For the CNN-based feature extraction of the time-series signal, representative research on feature extraction directly on one-dimensional signals can be found in [24–26]. Moreover, there are reports [27–29] on feature extraction based on two-dimensional images converted from one-dimensional signals. However, CNN-based methods require supervised learning based on a large number of labeled samples, which is not suitable for the situation that relies heavily on sufficient fastener looseness samples. Also, the above feature extraction methods are difficult to fully grasp or retain the spatial information between sampling points in the original one-dimensional signal. In contrast, the convolutional autoencoder (CAE) network [30] has low dependence on labeled samples for training; that is, CAE networks only need a small number of labeled samples for classification research on the dataset of interest [31,32]. Additionally, despite the lack of practical engineering verification cases concerning the signal dimensional conversion, it has been reported that the encoding operation of a one-dimensional signal based on a pseudo-Hilbert scan can theoretically preserve more of the sample's original feature [33–35]. This means that the encoding results of the two-dimensional images are beneficial to the signal feature extraction based on the CAE network.

Therefore, the purpose of this paper is to propose a method for identifying the looseness of subway fasteners based on the CAE network combined with the pseudo-Hilbert scan for the distributed vibration response detected by the ultra-weak FBG sensing array. That is, the original one-dimensional samples are converted into two-dimensional images through the pseudo-Hilbert scan, and then the converted results are used as inputs of the CAE network to perform the study of fastener looseness identification. The design and arrangement of the field experiment used to generate the fastener looseness dataset detected by the ultra-weak FBG sensing array make up the second part of this paper, followed by methodology details for identifying the looseness of subway fasteners, including the pseudo-Hilbert scan operation and the descriptions of CAE network architecture. Finally, the effectiveness and performance superiority of the proposed method are primarily quantified by accuracy, precision, recall, and F1-score, and the ability to distinguish target signals is further visualized by t-distributed stochastic neighbor embedding (t-SNE) [36].

## 2. Field Experiment for Generating the Fastener Looseness Dataset

### 2.1. Background of Vibration Signal Acquisition

The vibration signals used in this study were derived from the monitoring data of an actual subway tunnel structure. Before the operation of the subway, an ultra-weak FBG

sensing optic fiber with armored protection using a layer-stranding structure with a loose tube was fixed along the track bed surface of the selected tunnel segments. As shown in Figure 1, the monitoring area covers three underground stations of the subway line, with a total length of nearly three kilometers. The shallow groove embedding was adopted to affix the sensing array to secure a better vibration response of the track bed. The effect of this fixation method was discussed in [12]. The previous study [37] revealed the repeatability of such a sensor is around 3.41 nε. According to the 5 meters spatial resolution of the probes in the sensing optic fiber, more than 500 consecutive regions monitored along the track bed can feedback the structural vibration response based on the interrogated address of the light interference [19]. When a train passed, the structural vibration response triggered in each monitoring area was acquired at a 1 kHz sampling rate. The collected data was transmitted to the remote monitoring center for processing by the demodulator and server.

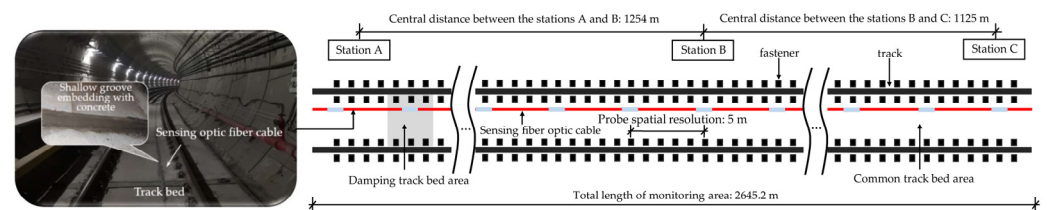


**Figure 1.** Field deployment of the ultra-weak FBG sensing array for acquiring vibration responses of track beds.

## 2.2. Design and Arrangement of Experimental Cases

At present, the subway line has already been in operation. To secure the safety of train operations on the following day, various inspections are usually conducted during the subway outage in the early hours of the morning. Therefore, the field experiment for collecting the dataset of fastener looseness was performed in this inspection window. As shown in Table 1, the distributed vibration responses of the track bed corresponding to three states were collected in total in the field test.

**Table 1.** Test time record in situ under three fastener states.

State Number	Fastener State	Driving Direction	Travel Time
1	Before looseness	Station B→Station C	0:58 a.m.–1:01 a.m.
		Station C→Station B	1:04 a.m.–1:07 a.m.
		Station B→Station C	1:10 a.m.–1:13 a.m.
		Station C→Station B	1:16 a.m.–1:19 a.m.
2	After looseness	Station B→Station C	1:34 a.m.–1:37 a.m.
		Station C→Station B	1:40 a.m.–1:43 a.m.
		Station B→Station C	1:46 a.m.–1:49 a.m.
		Station C→Station B	1:52 a.m.–1:55 a.m.
3	Retighten	Station B→Station C	2:06 a.m.–2:09 a.m.
		Station C→Station B	2:12 a.m.–2:15 a.m.
		Station B→Station C	2:18 a.m.–2:21 a.m.
		Station C→Station B	2:23 a.m.–2:26 a.m.

Note: (a) loosen fastener moments in monitoring areas #172, #164, and #160 were 1:22 a.m., 1:23 a.m. and 1:25 a.m., respectively. (b) retighten fastener moments in monitoring areas #160, #164, and #172 were 1:58 a.m., 2:00 a.m., and 2:02 a.m., respectively.

The three locations within monitoring areas #160, #164, and #172 shown in Figure 2 were randomly selected to perform fastener looseness. The selected sites are all located in the common track bed area, which accounts for the majority of the subway lines. The

rail inspection vehicle with a single carriage of about 5 meters in length was utilized to excite the vibration responses of the track bed under the three test states illustrated in Table 1. In each location, a crowbar was employed to manually loosen or tighten a pair of fasteners symmetrical on both sides of the track. To collect more samples within the limited experimental period, for fastener states 2 and 3 in Table 1, the 6 fasteners in the three locations were loosened or tightened together. Moreover, in areas covering the fasteners of interest, the rail inspection vehicle passed twice in two driving directions at a speed below 25 km/h, respectively. To ensure the quality of the collected signals, the vehicle stopped for 3 min each time it arrived at the station and then traveled in the direction specified in Table 1.

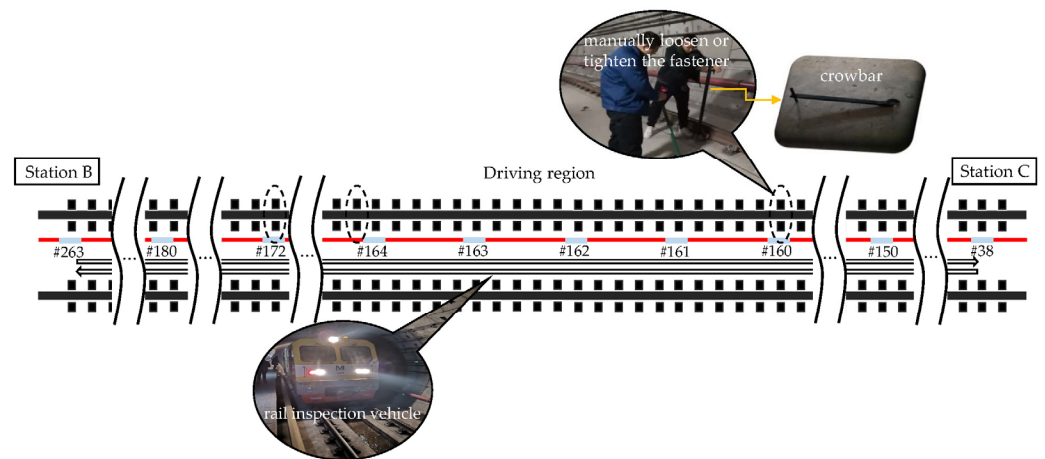


**Figure 2.** Position of the selected fasteners and detection area of the ultra-weak FBG sensing array.

### 2.3. Dataset and Its Division and Usage

According to the field records in Table 1, 12 groups of distributed vibration signals of the track bed structure caused by the passage of the rail inspection vehicle were collected. The vibration responses of the track bed within the range of #150 to #180 in the monitoring areas were selected to establish the dataset for the subsequent study. Among them, the signals in regions #160, #164, and #172 corresponding to fastener state 2 in Table 1 were considered to have fastener looseness characteristics. The responses under fastener states 1 and 3 for regions #160, #164, and #172, along with the vibration responses from the other regions, together constituted the samples of fasteners in the normal state.

The raw output result for each record in Table 1 can be plotted as a waterfall diagram of the vibration response versus time and space under the vehicle moving loads between stations B and C. Based on Table 1, Figure 3 depicts the waterfall diagrams of monitoring areas from #150 to #180 corresponding to the three fastener states. Here, the driving records for illustrating the three fastener states in Figure 3 were randomly selected from Table 1 under the premise of maintaining a consistent driving direction. Unfortunately, from the subplots of Figure 3, it is difficult to distinguish the negative influence of loose fasteners on the distributed vibration of the track bed.

Since there were only 12 original samples of the loose state of the fasteners, data augmentation was performed on the vibration signals of the monitoring areas corresponding to the three fastener looseness positions. Specifically, taking the original vibration response stimulated by the vehicle in monitoring area #160 as an example shown in Figure 4, the enhanced signals were generated by window-by-window translation for the collected signal, and the shift interval of the translation window was set to a one second step. Additionally, the width of the window ensures that the main vibration characteristics caused by the passage of the rail inspection vehicle can be preserved. Based on this strategy, the vibration response concerning the monitoring area corresponding to each fastener looseness position was represented by 32 samples in this paper.

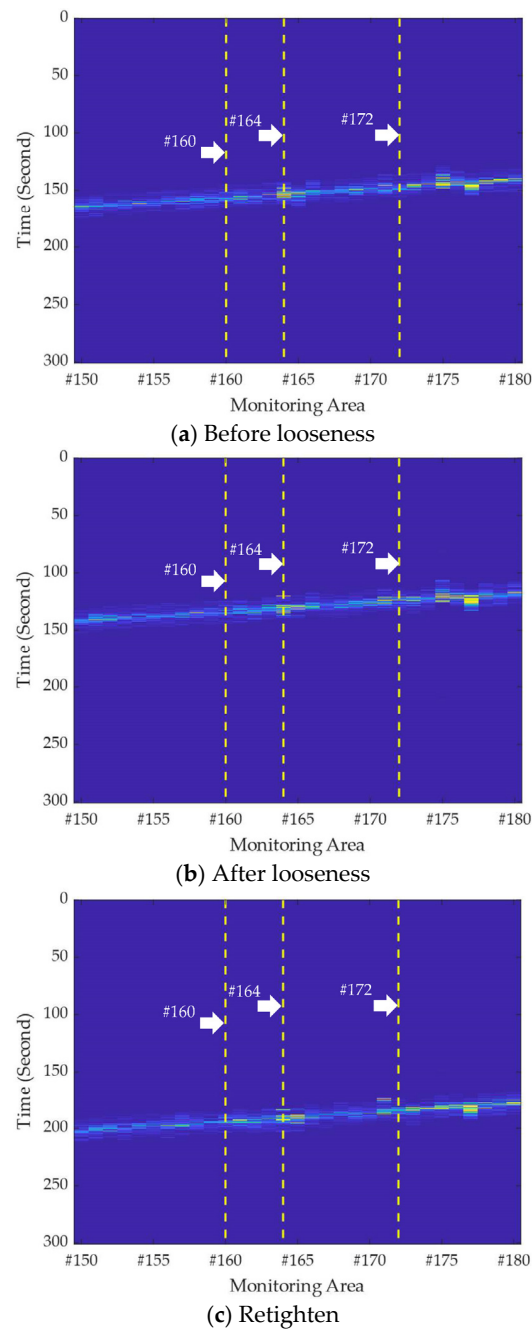


**Figure 3.** Vibration intensity versus space and time under the moving of rail inspection vehicle corresponding to (a–c) three fastener states.

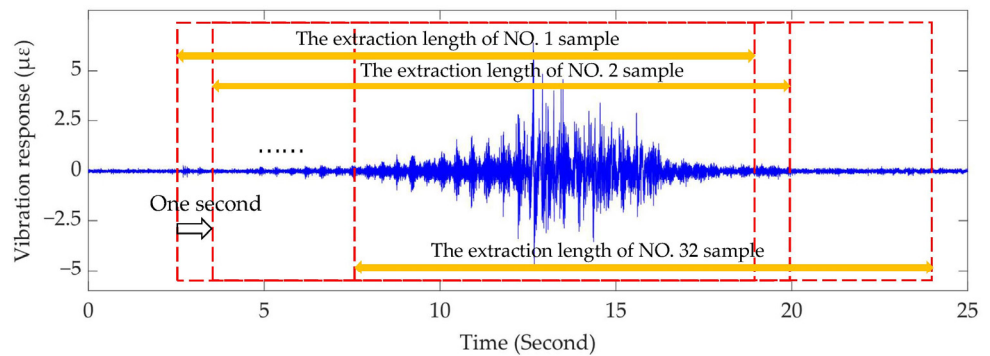


**Figure 4.** Data augmentation strategy for monitoring area #160 under fastener loose state.



The dataset of the normal state of the fastener came from two parts: the responses of the three monitoring areas #160, #164, and #172 under fastener states 1 and 3, and the responses of the remaining 31 monitoring areas under three specified states. Thus, the composition and size of the experimental dataset were given in Table 1. Here, to meet the consistency requirements of the CAE network for the dimension of the input sample, all samples described in Table 2 are kept at the same length with 20,164 sampling points.

**Table 2.** The composition and size of the experimental dataset.

Label	Sample Source	Sample Size	
A: Fastener in the loose state	#160	4→32	96
	#164	4→32	
	#172	4→32	
B: Fastener in the normal state	#160	4 + 4 = 8	396
	#164	4 + 4 = 8	
	#172	4 + 4 = 8	
	#150~#180 (except for #160, #164, and #172)	31 × 12 = 372	

To perform the subsequent study, the dataset described in Table 2 was divided into two parts to perform training and testing based on the commonly used ratio [38] of 7:3. As given in Table 3, the training set was used to perform the two-stage CAE network training. During the pre-training stage, all the training samples participate in the automatic extraction of hidden features of signals through unsupervised learning. Then, a fine-tuning of the network performance was performed in the second training stage of the CAE network. Here, to reduce the influence of asymmetry between sample sizes on fine-tuning results, the data balance between the two labels was considered. That is, 67 samples were randomly selected from the training dataset labeled B, together with all the training datasets labeled A, to form the labeled dataset for fine-tuning the network based on supervised learning. Moreover, to reduce the sensitivity of network performance to data partitioning and to obtain as much valid information as possible from the enhanced data, ten-fold cross-validation was used in this study. Additionally, a type of min-max normalization [39] was adopted to normalize all the sample amplitudes to the range of 0–1 to increase the learning efficiency of the proposed CAE network.

**Table 3.** The division and usage of the experimental dataset.

Dataset Division	Training Dataset Size		Test Dataset Size
	Pre-Training Stage	Fine-Tuning Stage	
Label A	67	67	29
Label B	277	67	119

### 3. Methodology for Identification of Fastener Looseness

#### 3.1. Pseudo-Hilbert Scan Operation

The pseudo-Hilbert scan can encode the original vibration response of the track bed by establishing a space-filling curve that matches the length of the one-dimensional sample sequence, namely, the length  $L$  and width  $W$  of the space-filling curve should meet Equation (1):

$$L \times W \geq N \quad (1)$$

where the result of  $L \times W$  is the minimum value that meets Equation (1),  $N$  represents the sequence length of the original sample, and  $L$ ,  $W$ , and  $N$  should all be integers.

According to the description in Section 2.3, the sequence length  $N$  of each original sample was set to 20,164. Therefore, the dimension shape of the space-filling curve can be set to  $142 \times 142$ . Under this condition, the result of  $L \times W$  was equal to  $N$ , which satisfied the instruction aforementioned. As well as that, the study in [40] revealed that the space-filling curve with equal length and width parameters ensured a better space clustering effect between the original sample points evaluated by mean square Euclidean distance [41]. In the implementation process, a null matrix of dimension  $142 \times 142$  for the pseudo-Hilbert scan was created. Then, the points within the null matrix that were used to form the initial space-filling curve were connected. According to the pseudo-Hilbert curve decomposition rule, the initial space-filling curve was gradually decomposed until obtaining the unit pseudo-Hilbert curve with a length or width of 1 or 2 [42]. Based on the Hilbert flipping operation [40], each basic unit pseudo-Hilbert curve was connected sequentially to form the pseudo-Hilbert curve as shown in Figure 5 for encoding the one-dimensional signal samples. The signal-to-image conversion operation based on the curve direction shown in Figure 5 can generate the input expression of the subsequent CAE network, where the evolution processes of the step-by-step decomposition and the sub-region connection are represented by different color blocks.

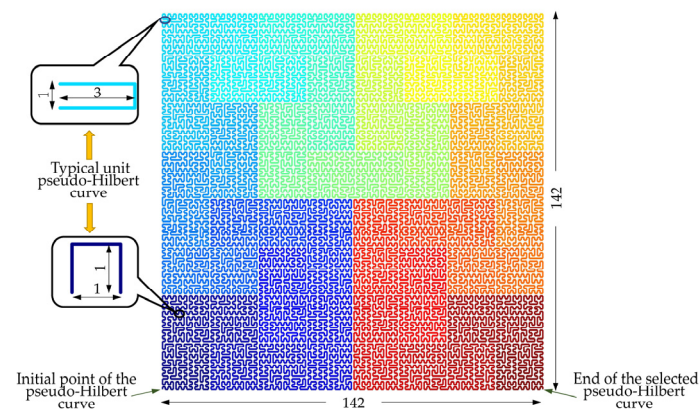


**Figure 5.** The pseudo-Hilbert curve for encoding the one-dimensional vibration response.

### 3.2. Establishment of CAE Network

Based on the report in [30,43] and the current experimental hardware environment (Dell PowerEdge T630 server) that was composed of a graphics processing unit (GPU) core (GTX 1080 Ti) with twelve 2.20 GHz processors (Intel Xeon E5-2650 v4), as shown in Figure 6, the proposed CAE network consisting of two training stages was established. Both for the pre-training and fine-tuning stages, the converted samples with the dimension of  $142 \times 142 \times 1$  processed by the pseudo-Hilbert scan were put into the input layer. In the pre-training stage, the established network used 2 convolution layers, 1 flatten layer, 3 linear layers, 1 unflatten layer, and 2 deconvolution layers in sequence to implement the encoding and decoding process for input samples. The goal of network training in this stage was to ensure that the prediction error exhibited a rather weak fluctuation, that is, to ensure that the difference between the predicted sequence and the input normal sample was small. During the feature extraction process based on unsupervised learning, the training dataset defined in Table 3 was used to preliminarily search the hyperparameters of the proposed CAE network. To suppress the occurrence of overfitting, rectified linear units [44] were used as an activation function and were added after each convolutional layer. Here, the number of neurons in each layer was derived through trial and error, assisted by grid searching [45]. In the fine-tuning stage, based on the balance training dataset defined in Table 3, the softmax layer and Label layer were added at the end of the encoding process in the pre-training network to perform hyperparameter fine-tuning based on supervised learning. To meet the training objective, adaptive moment estimation [46] was selected as the optimization algorithm of the network.



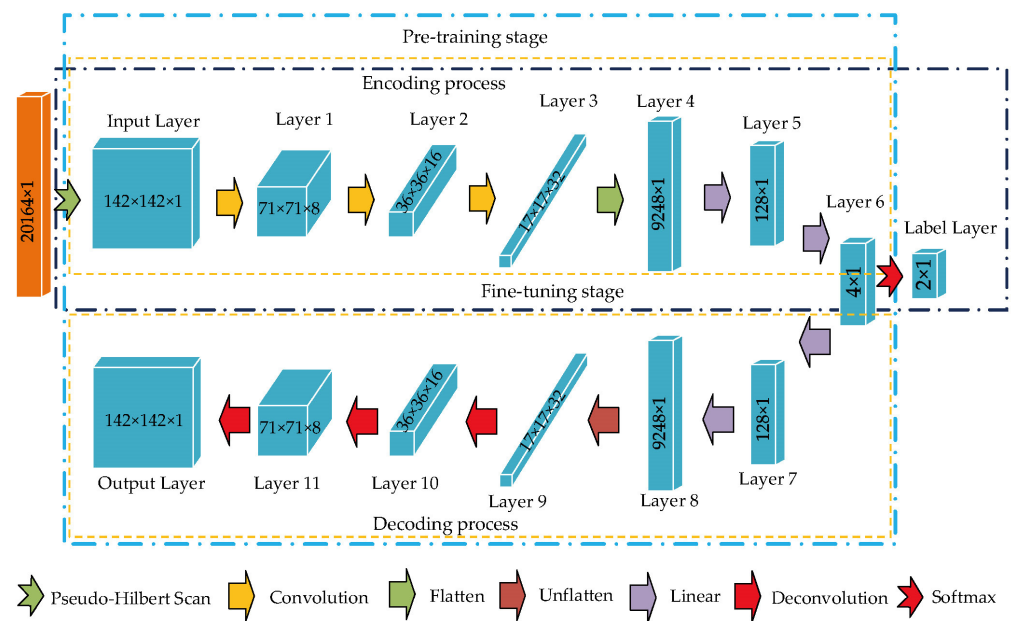
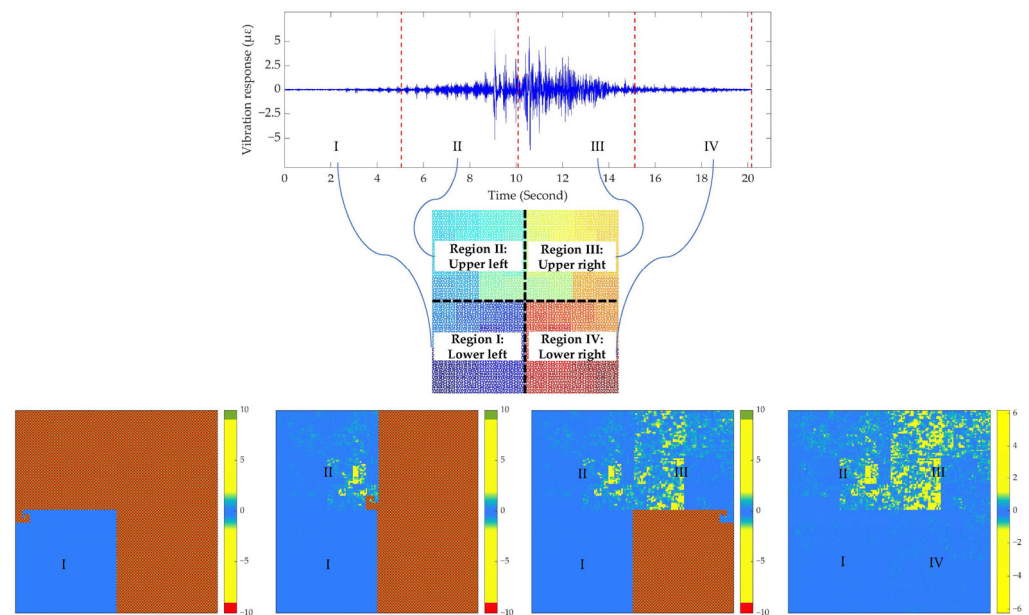


Figure 6. The proposed two-stage training CAE network architecture.

#### 4. Results, Analysis, and Discussion

Based on the pseudo-Hilbert scanning operation, the responses of the sampling points of the vibration signal were sequentially placed along the curve direction depicted in Figure 5. Then, the two-dimensional image with a dimension of  $142 \times 142$  serving as the input of the CAE network can be obtained. For the convenience of explanation, since the direction of the filling curve in Figure 5 starts from the lower left, then passes through the upper left and right regions, and finally ends at the lower right, the conversion process of signal-to-image can be illustrated by the evolution of four images in the bottom part of Figure 7. Specifically, the original vibration response of the track bed excited by the vehicle in each monitoring area can be viewed as consisting of four equal-length parts. Each one-dimensional signal sequence with a length of 5041 was converted to a two-dimensional image with a dimension of  $71 \times 71$ . It can be observed that the signals in regions II and III are more pronounced after the operation, while the conversion results in regions I and IV indicated by warm colors are not conspicuous, which conforms to the response amplitude distribution of the original signal. The image on the right side of the bottom part of Figure 7 was the final conversion result, which was used as the input of the CAE network.

According to the design in Table 3 and Figure 6, network training and testing were performed sequentially based on encoded samples under ten-fold cross-validation. With the current hardware configuration, the training runtime for the proposed network in each fold was approximately 3 h 58 min. The computation time was mainly consumed in the training phase, and the recognition prediction took only 2.43 s. For the test dataset defined in Table 3, the performance of the established CAE network was assessed by accuracy, precision, recall, and F1-score that have been widely used in the field of machine learning [47,48], and the corresponding indicator results were the average of ten-fold cross-validation and given in Table 4. From the results in Table 4, the overall performance of the network in distinguishing fastener looseness behaves well. However, directly adopting metric-based assessment is sometimes not the most appropriate choice for intuitively understanding or demonstrating network performance.



**Figure 7.** Pseudo-Hilbert scan results of a typical subway track bed vibration signal.

**Table 4.** Performance evaluation of the CAE network from four indicators in the case of the test dataset.

Indicator	Accuracy	Precision	Recall	F1-Score
Result	0.8784	0.9902	0.8571	0.9189

To visualize the classification advantage of the CAE network proposed in this paper, the final features compressed in Layer 6 in Figure 6 were first extracted and then converted into the clustering result of a two-dimensional plane based on the t-SNE technique [49]. If the clustering effect is good, it can be considered that the established training network has a strong ability to distinguish different states of fasteners. Under ten-fold cross-validation, the typical clustering results of the vibration signals of the track bed representing the two fastener states are shown in Figure 8. Here, the worst clustering effect in the ten-repetition test was selected as the typical result. It can be observed that fastener states were clustered into two categories. Specifically, the samples reflecting loose fasteners were distributed in an ellipse topology. Moreover, it can be inferred that at least 87.39% of the samples representing the normal state of fasteners were concentrated in the center of the ellipse. Although the effect was presented in different ways, the proportion of clusters from the visualization result based on the dimensionality-reduction algorithm agreed well with the confusion matrix conclusion shown in Figure 9, which verified that the proposed CAE network was able to identify the loose state of subway fasteners.

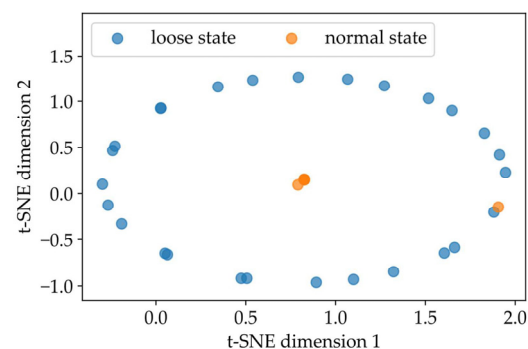


**Figure 8.** Clustering visualization results of fastener state feature based on t-SNE.

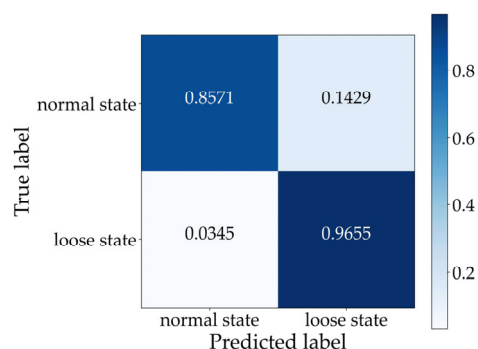


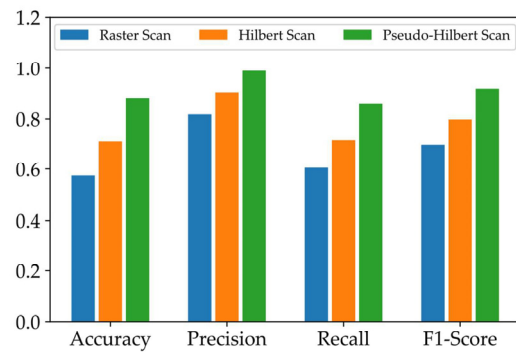
**Figure 9.** Confusion matrix of the proposed CAE network in the case of the test dataset.

In addition, the raster scan and the Hilbert scan, two commonly used methods that can convert one-dimensional signals into two-dimensional images [50], were selected to compare with the results of the pseudo-Hilbert scan used in this paper. For the training and test samples derived from the raster scan, the same network structure in Figure 6 was used to carry out the performance evaluation. Due to the specific coding rule of the Hilbert scan [51], the vibration samples with the original sequence length of 20,164 were encoded into the shape of  $256 \times 256$ . That is, during training and testing, the network layer structure used for the Hilbert scan was similar to Figure 6 except that the dimensions of the input layer, output layer, and partial intermediate layers for matching encoding and decoding were modified. Figure 10a depicts the comparison results after ten-fold cross-validation using the same four indicators from Table 4. It can be seen that the result of the pseudo-Hilbert scan outperformed those of the other two comparison methods, and the results of the raster scan were the least ideal. Based on the similar CAE network structure, the four indicators (accuracy, precision, recall, and F1-score) as shown in Figure 10b used for performance evaluation based on the pseudo-Hilbert scan were at least 23.8%, 9.5%, 20.0%, and 21.1% higher than those of the comparison methods, respectively. Moreover, the typical visualization results based on t-SNE are shown in Figure 11. The reason for the poor effect of the raster scan can be revealed in Figure 11a. Although two clusters were formed, it was obvious that each cluster area was mixed with different fastener states, which means the clustering result is chaotic. The typical topology result based on the Hilbert scan shown in Figure 11b derived from the best clustering effect of cross-validation and behaved similarly to that in Figure 8. However, only 75.63% of the samples representing the normal state of the fastener were concentrated in the center of the ellipse, which was lower than the minimum 87.39% ratio shown in Figure 8. Thus, the results reflected in Figure 11 also demonstrated that the proposed method had a better ability to identify the fastener looseness.

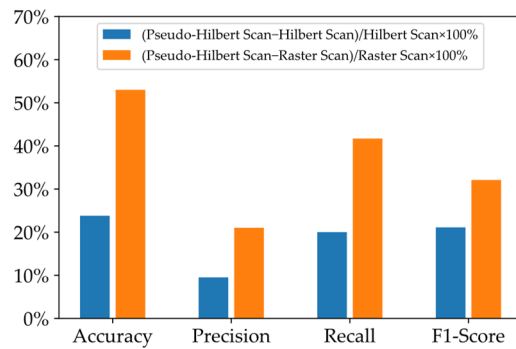
Based on the above results and analysis, Table 5 gives the performance comparison between the proposed CAE network combining pseudo-Hilbert scan and the similar network combining the other two scan techniques in terms of four machine learning indicators and t-SNE-based cluster ability. From the quantitative results, the method performance proposed in this paper is significantly better than that of conventional techniques.

**Table 5.** Performance comparison based on result analysis and discussion.

Item	Accuracy	Precision	Recall	F1-Score	Identifiability
Pseudo-Hilbert scan	0.8784	0.9902	0.8571	0.9189	87.39%
Raster scan	0.5743	0.8181	0.605	0.6957	chaos
Hilbert scan	0.7095	0.9043	0.7143	0.7589	75.63%

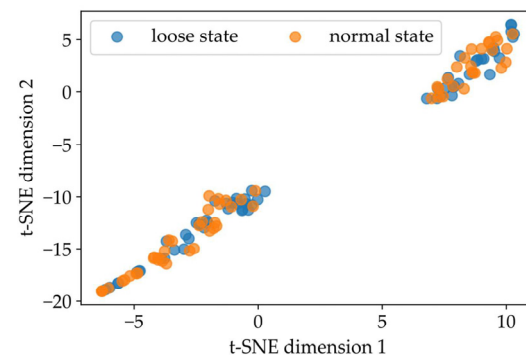


(a)

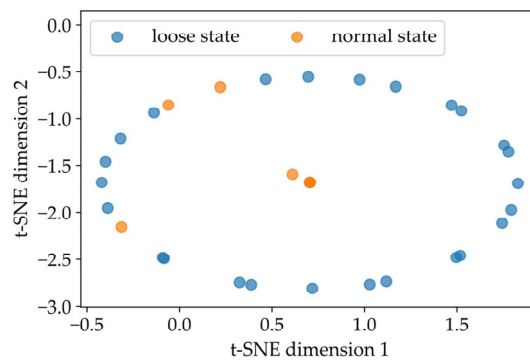


(b)

**Figure 10.** Results of (a) four indicators for evaluating network performance under different scanning methods and (b) performance superiority of pseudo-Hilbert scan.



(a) Raster scan



(b) Hilbert scan

**Figure 11.** Clustering visualization results of fastener state feature of (a) Raster scan and (b) Hilbert scan based on t-SNE.

## 5. Conclusions

This paper reports a method aimed at identifying the subway fastener looseness based on the experimental dataset of the track bed vibration detected by the ultra-weak FBG sensing array. To the best of our knowledge, this is the first study into the looseness identification of the track fastener through the CAE network combined with the pseudo-Hilbert scan, in which the limited but precious dataset came from practical engineering. The performance indicators of the proposed methodology in terms of accuracy, precision, recall, and F1-score were at least 23.8%, 9.5%, 20.0%, and 21.1% higher than those of the traditional techniques involved in the comparison. The visualization results from t-SNE also demonstrated that the method adopted in this paper had a strong ability to extract fastener state features and led the comparison techniques by at least 11.76%. Thus, it is believed that the current study will motivate future exploration into the detection of other undesirable track states through the distributed vibration response of the track bed. However, some limitations are worth noting. Although the recognition effect has been verified experimentally, it needs to be stressed that the approved area and duration for the organized field test in this paper were constrained by the regulations of the subway operation management. Therefore, the established two-stage CAE network architecture in the proposed method still deserves to be further improved by more unknown types and degrees of fastener looseness events. When facing datasets with more noise and establishing more complex deep learning networks, data preprocessing and hyperparameter optimization based on the Bayesian method [52–54] may be a viable alternative. Moreover, to prevent the risk of sudden intrusion into the subway line due to the excitation of vehicle moving load when the fasteners were in a semi-loose state, this paper only discussed the identification of the complete looseness state of the fasteners. That is, the selected fasteners were moved away from the subway line immediately after being manually loosened with the crowbar. Thus, the effectiveness based on the strategy proposed in this paper for identifying the fastener in a semi-loose state deserves further attention. For the above concerns, it is necessary to further study the experiment scheme suitable for collecting more types of samples of track distribution vibration in future work, which may be helpful for the study in the areas of identification of the track bed damage and train wheel fault.

**Author Contributions:** Conceptualization, S.L.; data curation, L.J.; funding acquisition, S.L. and J.J.; investigation, H.W.; methodology, L.J. and Q.N.; project administration, H.W.; resources, S.L.; supervision, L.S.; validation, S.L.; writing—original draft, L.J.; writing—review and editing, S.L. and Q.N. All authors have read and agreed to the published version of the manuscript.

**Funding:** This research was funded by the National Natural Science Foundation of China, grant numbers 61875155 and 52108472.

**Institutional Review Board Statement:** Not applicable.

**Informed Consent Statement:** Not applicable.

**Data Availability Statement:** The data presented in this study are available on request from the corresponding author.

**Acknowledgments:** The research work reported in this paper was supported by the National Engineering Research Center of Fiber Optic Sensing Technology and Networks, Wuhan University of Technology, and the Smart Nanocomposites Laboratory, University of California, Irvine.

**Conflicts of Interest:** The authors declare no conflict of interest.

## References

1. Nordmark, A. Fire and life safety for underground facilities: Present status of fire and life safety principles related to underground facilities. *Tunn. Undergr. Space Technol.* **1998**, *13*, 217–269. [[CrossRef](#)]
2. Liu, Z.; Kim, A.K. Review of recent developments in fire detection technologies. *J. Fire Prot. Eng.* **2003**, *13*, 129–151. [[CrossRef](#)]
3. Jiang, D.; Zhou, C.; Yang, M.; Li, S.; Wang, H. Research on optic fiber sensing engineering technology. In Proceedings of the 22nd International Conference on Optical Fiber Sensors, Beijing, China, 15–19 October 2012.



4. Pamukcu, S.; Cheng, L.; Pervizpour, M. Chapter 1—Introduction and overview of underground sensing for sustainable response. In *Underground Sensing. Monitoring and Hazard Detection for Environment and Infrastructure*, 1st ed.; Pamukcu, S., Cheng, L., Eds.; Academic Press: Cambridge, MA, USA, 2018; pp. 1–42.
5. Soga, K.; Kechavarzi, C.; Pelecanos, L.; Battista, N.; Williamson, M.; Gue, C.Y.; Murro, V.D.; Elshafie, M.; Monzón-Hernández, D., Sr.; Bustos, E.; et al. Chapter 6—Fiber-optic underground sensor networks. In *Underground Sensing. Monitoring and Hazard Detection for Environment and Infrastructure*, 1st ed.; Pamukcu, S., Cheng, L., Eds.; Academic Press: Cambridge, MA, USA, 2018; pp. 287–356.
6. Chen, X.; Li, X.; Zhu, H. Condition evaluation of urban metro shield tunnels in Shanghai through multiple indicators multiple causes model combined with multiple regression method. *Undergr. Space Technol.* **2019**, *85*, 170–181. [[CrossRef](#)]
7. Das, S.; Saha, P. A review of some advanced sensors used for health diagnosis of civil engineering structures. *Meas. J. Int. Meas. Confed.* **2018**, *129*, 68–90. [[CrossRef](#)]
8. Huang, J.; Zhang, W.; Huang, W.; Wang, L.; Luo, Y. High-resolution fiber optic seismic sensor array for intrusion detection of subway tunnel. In Proceedings of the 2018 Asia Communications and Photonics Conference (ACP), Hangzhou, China, 26–29 October 2018.
9. Yu, Z.; Liu, F.; Yuan, Y.; Li, S.; Li, Z. Signal processing for time domain wavelengths of ultra-weak FBGs array in perimeter security monitoring based on spark streaming. *Sensors* **2018**, *18*, 2937. [[CrossRef](#)]
10. Hoentsch, J.; Scholz, S. Reliable detection of security camera misalignment in urban rail environments. In Proceedings of the 2018 Joint Rail Conference, JRC 2018, Pittsburgh, PA, USA, 19–20 April 2018.
11. Gan, W.; Li, S.; Li, Z.; Sun, L. Identification of ground intrusion in underground structures based on distributed structural vibration detected by ultra-weak FBG sensing technology. *Sensors* **2019**, *19*, 2160. [[CrossRef](#)]
12. Nan, Q.; Li, S.; Yao, Y.; Li, Z.; Wang, H.; Wang, L.; Sun, L. A novel monitoring approach for train tracking and incursion detection in underground structures based on ultra-weak FBG sensing array. *Sensors* **2019**, *19*, 2666. [[CrossRef](#)]
13. Remennikov, A.M.; Kaewunruen, S. A review of loading conditions for railway track structures due to train and track vertical interaction. *J. Struct. Control Health Monit.* **2008**, *15*, 207–234. [[CrossRef](#)]
14. Jun, X.; Qingyuan, Z. A study on mechanical mechanism of train derailment and preventive measures for derailment. *Veh. Syst. Dyn.* **2005**, *43*, 121–147. [[CrossRef](#)]
15. Kaewunruen, S.; Osman, M.H.; Hao Cheng Eric, W. Risk-based maintenance planning for rail fastening systems. *ASCE-ASME J. Risk Uncertain. Eng. Syst. Part A Civ. Eng.* **2019**, *5*, 04019007. [[CrossRef](#)]
16. Ikshwaku, S.; Srinivasan, A.; Varghese, A.; Gubbi, J. Railway corridor monitoring using deep drone vision. In *Computational Intelligence: Theories, Applications and Future Directions—Volume II. Advances in Intelligent Systems and Computing*, 1st ed.; Verma, N., Ghosh, A.K., Eds.; Springer: Singapore, 2018; pp. 361–372.
17. Wei, X.; Yang, Z.; Liu, Y.; Wei, D.; Jia, L.; Li, Y. Railway track fastener defect detection based on image processing and deep learning techniques: A comparative study. *Eng. Appl. Artif. Intell.* **2019**, *80*, 66–81. [[CrossRef](#)]
18. Li, S.; Zuo, X.; Li, Z.; Wang, H.; Sun, L. Combining SDAE network with improved DTW algorithm for similarity measure of ultra-weak FBG vibration responses in underground structures. *Sensors* **2020**, *20*, 2179. [[CrossRef](#)]
19. Luo, Z.; Wen, H.; Guo, H.; Yang, M. A time-and wavelength-division multiplexing sensor network with ultra-weak fiber Bragg gratings. *Opt. Express* **2013**, *21*, 22799–22807. [[CrossRef](#)]
20. Wang, S.; Liu, D.; Yang, Z.; Feng, C.; Yao, R. A convolutional neural network image classification based on extreme learning machine. *IAENG Int. J. Comput. Sci.* **2021**, *48*, 1–5.
21. Ye, C.; Yin, Z.; Zhao, M.; Tian, Y.; Sun, Z. Identification of mental fatigue levels in a language understanding task based on multi-domain EEG features and an ensemble convolutional neural network. *Biomed. Signal Process. Control* **2022**, *72*, 103360. [[CrossRef](#)]
22. Fan, Q. The application of minority music style recognition based on deep convolution loop neural network. *Wireless Commun. Mobile Comput.* **2022**, *2022*, 4556135. [[CrossRef](#)]
23. Tang, Z.; Chen, Z.; Bao, Y.; Li, H. Convolutional neural network-based data anomaly detection method using multiple information for structural health monitoring. *J. Struct. Control Health Monit.* **2019**, *26*, 2296. [[CrossRef](#)]
24. Li, S.; Sun, L. Detectability of bridge-structural damage based on fiber-optic sensing through deep-convolutional neural networks. *J. Bridge Eng.* **2020**, *25*, 04020012. [[CrossRef](#)]
25. Abdeljaber, O.; Avci, O.; Kiranyaz, M.S.; Boashash, B.; Sodano, H.; Inman, D.J. 1-D CNNs for structural damage detection: Verification on a structural health monitoring benchmark data. *Neurocomputing* **2018**, *275*, 1308–1317. [[CrossRef](#)]
26. Dhar, P.; Garg, V.K.; Rahman, M.A. Enhanced feature extraction-based CNN approach for epileptic seizure detection from EEG signals. *J. Healthc. Eng.* **2022**, *2022*, 3491828. [[CrossRef](#)]
27. Hasan, M.J.; Islam, M.M.M.; Kim, J. Acoustic spectral imaging and transfer learning for reliable bearing fault diagnosis under variable speed conditions. *Meas. J. Int. Meas. Confed.* **2019**, *138*, 620–631. [[CrossRef](#)]
28. Li, Y.; Cheng, G.; Pang, Y.; Kuai, M. Planetary gear fault diagnosis via feature image extraction based on multi central frequencies and vibration signal frequency spectrum. *Sensors* **2018**, *18*, 1735. [[CrossRef](#)]
29. Hoang, D.; Kang, H. Rolling element bearing fault diagnosis using convolutional neural network and vibration image. *Cogn. Syst. Res.* **2019**, *53*, 42–50. [[CrossRef](#)]



30. Yu, H.; Tao, J.; Qin, C.; Liu, M.; Xiao, D.; Sun, H.; Liu, C. A novel constrained dense convolutional autoencoder and DNN-based semi-supervised method for shield machine tunnel geological formation recognition. *Mech. Syst. Signal Process.* **2022**, *165*, 108353. [[CrossRef](#)]
31. Zhang, H.; Tang, W.; Zhang, L.; Li, P.; Gu, D. Defect detection of yarn-dyed shirts based on denoising convolutional self-encoder. In Proceedings of the 8th IEEE Data Driven Control and Learning Systems Conference, Dali, China, 24–27 May 2019.
32. Zhang, E.; Seiler, S.; Chen, M.; Lu, W.; Gu, X. Boundary-aware semi-supervised deep learning for breast ultrasound computer-aided diagnosis. In Proceedings of the 41st Annual International Conference of the IEEE Engineering in Medicine and Biology Society, Berlin, Germany, 23–27 July 2019.
33. Tsinganos, P.; Cornelis, B.; Cornelis, J.; Jansen, B.; Skodras, A. Hilbert sEMG data scanning for hand gesture recognition based on deep learning. *Neural Comput. Appl.* **2021**, *33*, 2645–2666. [[CrossRef](#)]
34. Kamata, S.; Bandoh, Y. Address generator of a pseudo-Hilbert scan in a rectangle region. In Proceedings of the 1997 International Conference on Image Processing, Santa Barbara, CA, USA, 26–29 October 1997.
35. Biswas, S. Hubert scan image compression. In Proceedings of the 15th International Conference on Pattern Recognition, Barcelona, Spain, 3–7 September 2000.
36. Lu, W.; Yan, X. Industrial process data visualization based on a deep enhanced t-distributed stochastic neighbor embedding neural network. *Assem. Autom.* **2022**, *42*, 268–277. [[CrossRef](#)]
37. Tong, Y.; Li, Z.; Wang, J.; Wang, H.; Yu, H. High-speed Mach-Zehnder-OTDR distributed optical fiber vibration sensor using medium-coherence laser. *Photonic Sens.* **2018**, *8*, 203–212. [[CrossRef](#)]
38. Sitaula, C.; Hossain, M.B. Attention-based VGG-16 model for COVID-19 chest X-ray image classification. *Appl. Intell.* **2021**, *51*, 2850–2863. [[CrossRef](#)] [[PubMed](#)]
39. Patro, S.G.K.; Sahu, K.K. Normalization: A preprocessing Stage. Available online: <https://arxiv.org/abs/1503.06462> (accessed on 22 July 2022).
40. Moon, B.; Jagadish, H.V.; Faloutsos, C.; Saltz, J.H. Analysis of the clustering properties of the Hilbert space-filling curve. *IEEE Trans. Knowl. Data Eng.* **2001**, *13*, 124–141. [[CrossRef](#)]
41. Zhang, J.; Kamata, S. A generalized 3-D Hilbert scan using look-up tables. *J. Visual Commun. Image Represent.* **2012**, *23*, 418–425. [[CrossRef](#)]
42. Zhang, J.; Kamata, S.; Ueshige, Y. A pseudo-Hilbert scan algorithm for arbitrarily-sized rectangle region. In Proceedings of the International Workshop on Intelligent Computing in Pattern Analysis/Synthesis, Xi'an, China, 26–27 August 2006.
43. Han, Z.; Li, J.; Zhang, B.; Hossain, M.M.; Xu, C. Prediction of combustion state through a semi-supervised learning model and flame imaging. *Fuel* **2021**, *289*, 119745. [[CrossRef](#)]
44. Nair, V.; Hinton, G.E. Rectified linear units improve restricted Boltzmann machines. In Proceedings of the 27th International Conference on Machine Learning, Haifa, Israel, 21–25 June 2010.
45. Lameski, P.; Zdravevski, E.; Mingov, R.; Kulakov, A. SVM parameter tuning with grid search and its impact on reduction of model over-fitting. In *Rough Sets, Fuzzy Sets, Data Mining, and Granular Computing*; Lecture Notes in Computer Science; Springer: Cham, Switzerland, 2015; Volume 9437, pp. 464–474.
46. Ruder, S. An Overview of Gradient Descent Optimization Algorithms. Available online: <https://arxiv.org/abs/1609.04747v2> (accessed on 22 July 2022).
47. Kuo, K.M.; Talley, P.C.; Chang, C.S. The accuracy of machine learning approaches using non-image data for the prediction of COVID-19: A meta-analysis. *Int. J. Med. Inf.* **2022**, *164*, 104791. [[CrossRef](#)]
48. Wang, R.; Li, J. Bayes test of precision, recall, and F1 measure for comparison of two natural language processing models. In Proceedings of the 57th Annual Meeting of the Association for Computational Linguistics, Florence, Italy, 28 July–2 August 2020.
49. Atangana Njock, P.G.; Shen, S.; Zhou, A.; Lyu, H. Evaluation of soil liquefaction using AI technology incorporating a coupled ENN/t-SNE model. *Soil Dyn. Earthqu. Eng.* **2020**, *130*, 105988. [[CrossRef](#)]
50. Bai, Y.; Feng, Y.; Wang, Y.; Dai, T.; Xia, S.; Jiang, Y. Hilbert-based Generative Defense for Adversarial Examples. In Proceedings of the 2019 IEEE/CVF International Conference on Computer Vision (ICCV), Seoul, Korea, 27 October–2 November 2019.
51. Kamata, S.; Eason, R.O.; Bandou, Y. A new algorithm for N-dimensional Hilbert scanning. *IEEE Trans. Image Process.* **1999**, *8*, 964–973. [[CrossRef](#)]
52. Zhang, Y.M.; Wang, H.; Mao, J.X.; Xu, Z.D.; Zhang, Y.F. Probabilistic framework with Bayesian optimization for predicting typhoon-induced dynamic responses of a long-span bridge. *J. Struct. Eng.* **2021**, *147*, 04020297. [[CrossRef](#)]
53. Zhang, Y.M.; Wang, H.; Bai, Y.; Mao, J.X.; Xu, Y.C. Bayesian Dynamic Regression for Reconstructing Missing Data in Structural Health Monitoring. *Struct. Health Monit.* **2022**. [[CrossRef](#)]
54. Wan, H.P.; Ni, Y.Q. Bayesian multi-task learning methodology for reconstruction of structural health monitoring data. *Struct. Health Monit.* **2019**, *18*, 1282–1309. [[CrossRef](#)]